Optical coherence elastography for measuring the deformation within glass fiber composite

Ping Liu,[1] Roger M. Groves,[1,*] and Rinze Benedictus[2]

[1]Aerospace Non-Destructive Testing Laboratory, Faculty of Aerospace Engineering, Delft University of Technology,
Kluyverweg 1, 2600 GB, Delft, The Netherlands

[2]Structural Integrity & Composites Group, Faculty of Aerospace Engineering, Delft University of Technology,
Kluyverweg 1, 2600 GB, Delft, The Netherlands

*Corresponding author: r.m.groves@tudelft.nl

Received 17 April 2014; revised 3 June 2014; accepted 23 June 2014;
posted 8 July 2014 (Doc. ID 209968); published 1 August 2014

Optical coherence elastography (OCE) has been applied to the study of microscopic deformation in biological tissue under compressive stress for more than a decade. In this paper, OCE has been extended for the first time, to the best of our knowledge, to deformation measurement in a glass fiber composite in the field of nondestructive testing. A customized optical coherence tomography system, combined with a mechanical loading setup, was developed to provide pairs of prestressed and stressed structural images. The speckle tracking algorithm, based on 2D cross correlation, was used to estimate the local displacements in micrometer scale. The algorithm was first evaluated by a test of rigid body translation. Then the experiments were carried out with the tensile test and three point bending on a set of glass fiber composites. The structural features and structural variations during the mechanical loadings are clearly observed with the presented displacement maps. The advantages and prospects for OCE application on glass fiber composites are discussed at the end of this paper.

OCIS codes: (110.4500) Optical coherence tomography; (100.6950) Tomographic image processing; (110.6150) Speckle imaging; (120.4290) Nondestructive testing.
http://dx.doi.org/10.1364/AO.53.005070

1. Introduction

In the area of experimental solid mechanics, deformation and strain measurement of materials and structures subjected to various loadings (e.g., mechanical loading or thermal loading) is an important task. Aside from the widely used pointwise strain gauge technique, various full-field noncontact optical methods, such as holography [1], speckle interferometry [2], moiré interferometry [3], and digital image correlation (DIC) [4], have been widely accepted and commonly used as powerful tools to analyze the mechanical properties of structures. However, all these techniques are developed for surface deformation measurement. Due to anisotropy or inhomogeneity of materials such as composites, the measurement of microscopic deformation within the structure is of interest for providing new information about the internal structural behavior under loading. So far, embedded fiber Bragg grating (FBG) sensors [5,6] have been proved to be well suited for accurate, localized, or distributed strain measurement in composite structures. However a major problem is that this type of technique is not able to provide a full field view of the strain distribution within the material.

Elastography [7] is a noninvasive medical image technique that can map the elastic properties of soft tissue. The local variations of the stiffness inside the tissue can be determined from the elastography maps, known as elastograms, which provide additional clinical information for diagnosis of various diseases. In the past 20 years, elastography has been

1559-128X/14/225070-08$15.00/0

extensively developed, largely based on ultrasound [8] and magnetic resonance imaging (MRI) [9]. However, the major drawback of ultrasound scanning and MRI is their relatively low spatial resolution. So far, with the advance of these techniques, high-frequency ultrasound has improved the imaging resolution to 25 μm [10], and MRI can reach 44 μm [11]. Nevertheless, these methods are still limited for the measurement of micromechanical properties.

Optical coherence tomography (OCT) [12] is a contactless and nondestructive imaging modality based on the principle of low coherence interferometry. OCT has an inherent spatial resolution of 1–15 μm [13], much better than ultrasound and MRI techniques. Optical coherence elastrography (OCE), an OCT-based elastrography, was first introduced by Schmitt [14] in 1998. It was used to detect the depth-resolved sample deformation induced by quasi-static compression. Benefiting from the high resolution of OCT, OCE has the potential to evaluate the elasticity of the sample with a spatial resolution and sensitivity that are out of the reach of ultrasound and MRI.

Inspired by the OCE applications on biological tissues [15–17], this paper aims to explore OCE to investigate glass fiber composites under mechanical loadings. The paper is structured as follows: Section 2 describes a customized OCT setup, loading system, and speckle tracking algorithm for displacement measurement. In Section 3, an evaluation of the designed OCE system is reported for rigid body translation. Then displacement maps are determined by applying the verified OCE technique on glass fiber composites under different mechanical loadings. In Section 4, the advantages and possible further improvements for OCE application on glass fiber composites are discussed. Finally, Section 5 concludes this paper.

2. Methods

A. Experimental Setup

A simplified schematic of an OCT system is shown in Fig. 1(a) [18]. The technique is based on low coherence interferometry and is implemented using a fiber-optic Michelson interferometer. The light beam from a superluminescent diode (SLD, FESL-1550-20-BTF, Frankfurt Laser Company, Germany) is coupled with a 3 dB fiber coupler and divided into sample and reference arms. Light backreflected from the sample and reference mirror is recombined and directed to a photo detector (PDB420C, Thorlabs GmbH, Germany). Due to the broadband bandwidth of the light source, the light from reference and sample arms will interfere coherently at the detector only if their optical pathlengths are matched to within the coherence length of the light source. By scanning the reference mirror, achieved by incorporating an optical delay line (ODL-650-MC, OZ Optics Ltd., Canada) in the reference arm, a set of interferometric signals will be detected as a function of the reference mirror position. This set corresponds to the axial distribution of the scattering interface within the specimen and refers to the A-scan. By shifting the probe beam with a translation stage (T-LS28M, Zaber Inc., Canada), a set of consecutive A-scans can be obtained. These A-scans are then combined to form a cross-sectional image of the structure, which is named the B-scan.

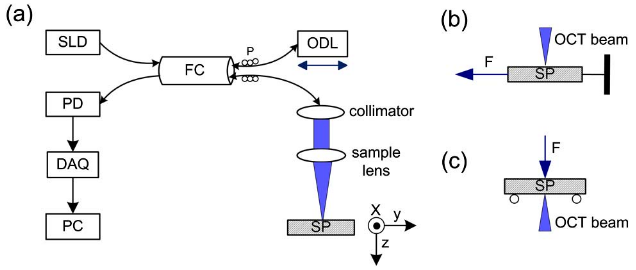

Fig. 1. Schematic setup for OCE application. (a) Customized fiber-optical OCT system. (b), (c) Tensile and three point bending tests on the specimen, respectively. SLD, superluminescent diode; FC, fiber coupler; P, polarization controller; ODL, optical delay line; PD, photo detector; SP, sample; DAQ, data acquisition board; F, force.

The specimens investigated in this paper are glass fiber composites with eight layers of 0/90° woven E-glass fiber in an epoxy resin. The dimensions of each specimen are 100 mm length, 10 mm width, and 2.15 mm thickness. In order to get a better penetration depth, the wavelength of the SLD is centered at 1550 nm, which has proved to be less scattering and gives deeper penetration in polymer-based material than the shorter wavelength used for biomedical applications [19]. The light source has a full width at half-maximum (FWHM) bandwidth of 60 nm, providing a theoretical axial resolution [20] of 17 μm in air and approximately 11 μm resolution in the polymer composite, with a 1.55 average refractive index taken into account. This index of refraction was estimated by calculating the ratio of the optical thickness, measured by OCT, to the real physical thickness, measured by a caliper. In the sample arm, the light beam exiting the optical fiber is collimated by a fiberport (F260APC-1550, Thorlabs GmbH, Germany) and then focused to the specimen by a achromatic doublet lens (AC254-030-C-ML, Thorlabs GmbH, Germany), resulting in a lateral resolution [21] of 20 μm.

To carry out the mechanical test, two loading systems, tensile test and three point bending, were designed, as shown in Figs. 1(b) and 1(c), respectively. During the tensile test, the rectangular specimen was clamped horizontally. One side of the specimen was fixed, while the other was driven by a linear actuator (NA23C60-T4, Zaber Inc., Canada). The distance between the two fixture points was 90 mm. In the three point bending test, two rods with a separation distance of 50 mm were in contact with the lower surface of the specimen. The same actuator provided the loading from the middle point on the opposite side of the specimen. In the both loading systems, OCT lateral scans were symmetrically distributed around the middle of the two fixture points.

The pairs of tomograms acquired before and after deformation were then analyzed to determine the displacement maps.

B. Image Processing Techniques

Similar to their ultrasonic counterparts, most OCE techniques rely on speckle tracking [22] to estimate the relative motion of subsurface structure imaged under different loading force. Phase-sensitive detection [23] is another methodology to measure the internal displacement, but it only works for a Fourier-domain OCT (FD-OCT) platform and cannot measure the lateral displacement. Typically, during speckle tracking, the pairs of OCT B-scan images from prestressed and stressed specimens are processed with the cross-correlation technique. The cross correlation coefficient, $R_{l,k}$, is defined by

$$R_{l,k}=\frac{\sum_{i=1}^{m_1}\sum_{j=1}^{m_2}(X_{i,j}-\bar{X})(Y_{i+l,j+k}-\bar{Y})}{\sqrt{\sum_{i=1}^{m_1}\sum_{j=1}^{m_2}(X_{i,j}-\bar{X})^2\sum_{i=1}^{m_1}\sum_{j=1}^{m_2}(Y_{i+l,j+k}-\bar{Y})^2}}, \qquad (1)$$

where $\bar{X}$ and $\bar{Y}$ are the mean pixel values in a predefined subset, $m_1 \times m_2$, on images X and Y, respectively. i and j are the axial and lateral locations of a given pixel in image X, while l and k are the corresponding pixel displacements in image Y. Over the search region, an array of correlation coefficients is calculated, and its peak value identifies the target destination.

Figure 2 defines the procedure for internal displacement measurement based on the cross-correlation approach. The displacements are estimated pixel by pixel until the processing window moves over the entire prestressed image. However, to guarantee the accuracy of the speckle tracking, regions where the magnitude of the interference signals falls below twice the level of the electronic noise are excluded from the analysis. The average of the electronic noise is obtained from the area where the structure is not imaged (e.g., above the specimen surface). A threshold for the maximum correlation coefficient is also set to eliminate the pixels that are not able to be tracked correctly. The threshold value is optimized to 0.25 in this paper by minimizing the difference between the calculated mean displacement and the actual one deduced from the translation of the actuator. Besides, the size of the processing window, $m_1 \times m_2$, is an important parameter in the tracking procedure. An optimization of the window size is discussed in Section 3.B. Finally a 2D median filter is applied to remove the random noise and thus improve the contrast of the displacement images.

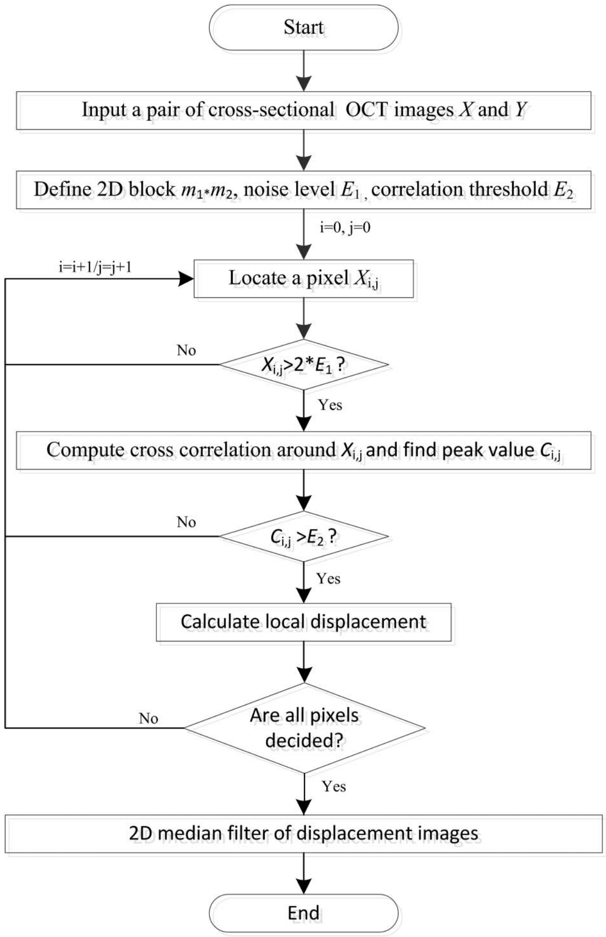

Fig. 2. Image processing steps for internal displacement estimation.

3. Results

A. Rigid Body Translation

A test of rigid body translation was introduced to evaluate the OCE system for the application of glass fiber composite. A pair of cross-sectional images were obtained before and after the specimen movement and are shown in Figs. 3(a) and 3(b). Both images are composed of 500 A-scans and have 10 mm length. The internal structures are shown by the optical reflectivity in logarithmic scale, as indicated by the

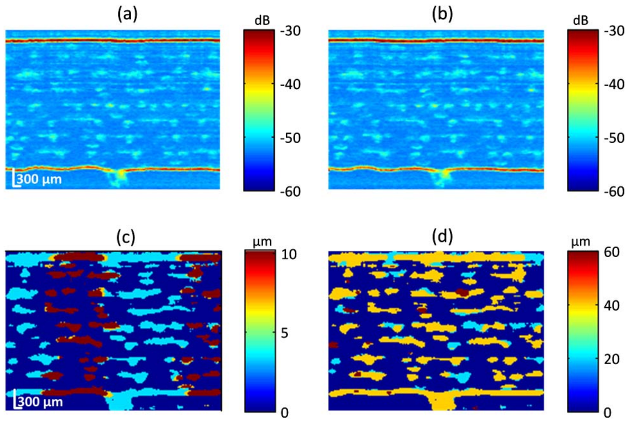

Fig. 3. OCE evaluation with a test of rigid body translation. (a), (b) Pair of structural images before and after translation, respectively. (c), (d) Calculated displacement maps in the axial and lateral directions, respectively.

Table 1. OCE System Accuracy Analysis

Orientation	$\bar{d}$/µm	d/µm	PE	RMSE/µm
Axial	6.6	6.8	2.9%	3.3
Lateral	39.4	40	1.5%	10.2

colorbar. Two bright lines as well as some lighter areas in between can be seen from both images, which indicate the surfaces and the fiber bundles within the specimen, respectively. From Figs. 3(a) and 3(b), the entire specimen was translated 6.8 µm axially and 40 µm laterally, equivalent to 2 pixels along both directions in the structural images. However, the difference of the two structural images can barely be observed. With the speckle tracking algorithm, the axial and lateral displacements were calculated, as shown in Figs. 3(c) and 3(d), respectively. Displacements at the edges of the structure images are neglected due to the lack of data for the processing window. The areas without any displacement in Figs. 3(c) and 3(d) indicate the locations without enough tracking speckles due to weak reflectivity. These mostly occur at the resin-rich areas.

Table 1 summarizes the OCE system accuracy by evaluating the percentage error (PE) and root mean square error (RMSE), given by

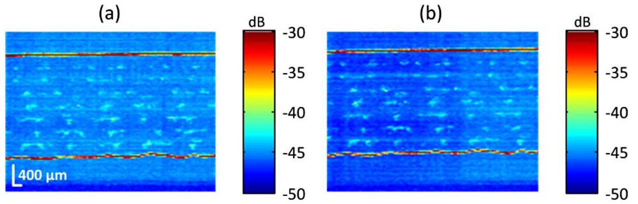

Fig. 4. Pair of cross-sectional images of a glass fiber composite (a) before and (b) after deformation. Both images were acquired from the same spatial location over a 10 mm length, composed of 500 A-scans.

$$\mathrm{PE} = \frac{|\bar{d} - d|}{d}, \tag{2}$$

$$\mathrm{RMSE} = \sqrt{\frac{1}{MN}\sum_{i=1}^{M}\sum_{j=1}^{N}(\hat{d}_{i,j} - d)^2}, \tag{3}$$

where $\hat{d}_{i,j}$ and $\bar{d}$ are the calculated local and mean displacements, respectively. d is the rigid body translation precisely controlled by the translation stages. $M \times N$ is the pixel size of the displacement maps. The areas with zero displacement because of untraceability were excluded from the statistics analysis. From the results summarized in Table 1, it is noticeable that the mean displacements in both the axial and lateral directions are extremely close to the actual physical translation. The PEs are 2.9% axially and 1.5% laterally, and the RMSEs are 3.3 and 10.2 µm, respectively. The higher lateral RMSE is due to the larger pixel interval (20 µm) in this direction. Actually the corresponding RMSEs in pixels are 1 axially and 0.5 laterally, which indicates a larger variation of the measured displacements in the axial direction. This can also be deduced from the inhomogeneous displacement map, as shown in Fig. 3(c). The higher axial measurement error could be attributed to the nonlinear sweeping of the reference mirror in the OCT setup, as evaluated in our previous publication [24]. The nonlinear sweeping mainly exists at the startup of the reference motor where acceleration occurs, so the A-scans could have some misalignment, which brings an extra measurement error in the axial direction.

B. Tensile Test

In the tensile test experiment, the specimen was stretched 500 µm overall, precisely controlled by

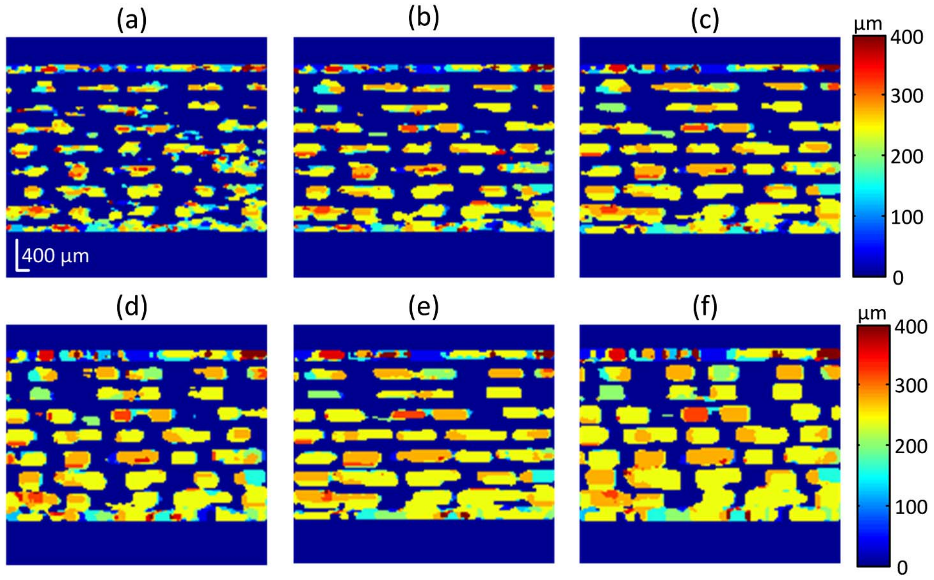

Fig. 5. Lateral displacement maps with processing window size (axial by lateral) (a) 20 ∗ 20, (b) 30 ∗ 30, (c) 40 ∗ 40, (d) 60 ∗ 30, (e) 50 ∗ 50, and (f) 80 ∗ 40. The areas with background color indicate where the signal-to-noise ratio is too low for the displacement calculation.

the actuator. Two cross-sectional images were recorded before and after the loading, as shown in Fig. 4. Both images were obtained by 500 A-scans in the same spatial region with 10 mm length, in the middle of the specimen along the stretch direction. The pair of images was processed to calculate the lateral displacement. In this research, the influence of processing window size for cross correlation was investigated. Figure 5 shows the calculated lateral displacement with processing window sizes of $20 * 20$, $30 * 30$, $40 * 40$, $60 * 30$, $50 * 50$, and $80 * 40$ pixels (depth by lateral). The unsquared window sizes were selected considering the structural images are $1000 * 500$ pixels (depth by lateral) overall. Larger window sizes were not used in this study due to the fact that they would not able to track the small particles in the images [25].

The mean displacements at different lateral locations can be calculated by averaging each axial line of the displacement maps. As an example, Fig. 6(a) shows the averaged displacement when the $50 * 50$ window size was applied for the correlation process. It can be seen that the calculated displacements are quite close to 250 μm, which is the theoretical average displacement of the imaging area located in the middle of the sample. The theoretical displacement is calculated based on the assumption that the specimen is isotopic and the stress is applied uniformly in the lateral direction, so the local lateral displacement d_l should be proportional to its physical distance to the fixed end of the specimen Δl, given by

$$d_l = \frac{500}{90000}\Delta l, \tag{4}$$

where 500 and 90,000 μm are the overall loading displacement and distance, respectively. To compare the measurement accuracy, the mean displacement and the RMSE were calculated for each window size, as shown in Figs. 6(b) and 6(c). It can be seen that with a processing window size of $50 * 50$, the calculated mean displacement is closest to the theoretical value and the RMSE reaches minimum. In this way the ideal window size can be determined and the same parameters were used for the rest of this study.

However, it is also noted, from Fig. 6(a), that it is difficult to observe the tendency of the variation in displacement with regard to the lateral distance. A major factor is the small displacement variation [approximately 55 μm based on Eq. (4)], relatively low lateral resolution, and pixel interval (20 μm) in the OCT images. Displacements of a fraction of a pixel are impossible to precisely track with the current approach. More detailed considerations of the measurement accuracy are discussed in Section 4.

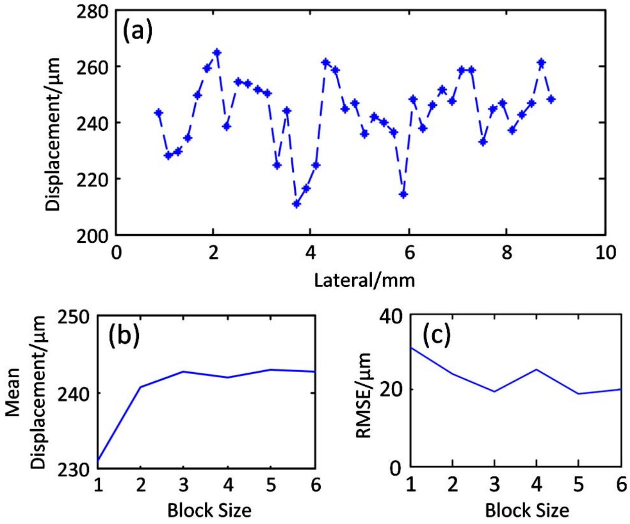

Fig. 6. (a) Mean displacement with regard to the lateral location, calculated by averaging each axial line of the displacement maps. (b), (c) Mean and RMSE of the lateral displacement with regard to the increased window size. Specifically, the block sizes 1 to 6 represent window sizes of $20 * 20$, $30 * 30$, $40 * 40$, $60 * 30$, $50 * 50$, and $80 * 40$, respectively.

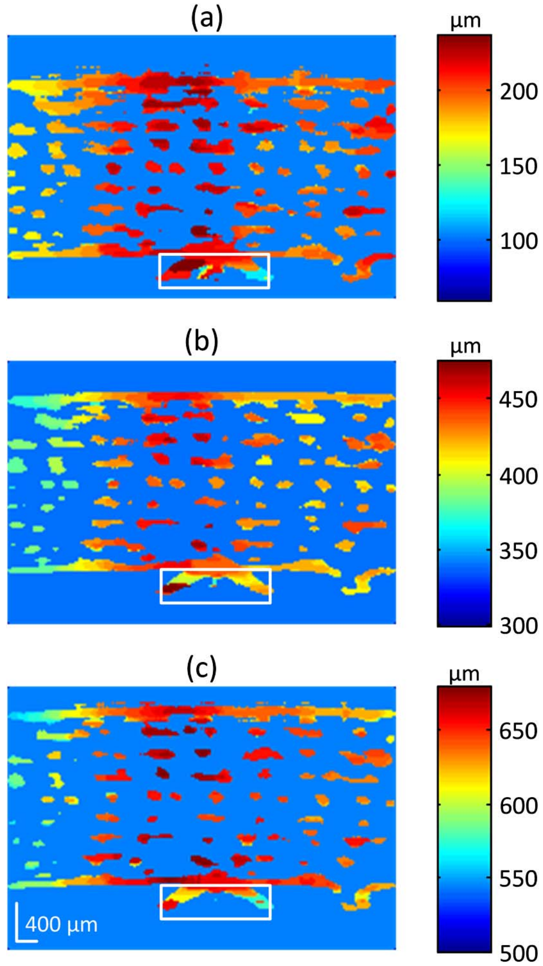

Fig. 7. Axial displacement maps from one cross-sectional structure of the glass fiber composite under three point bending test. The white frames indicate the location of the loading actuator. The incremental axial translation increases by 250 μm for each successive image (a)–(c).

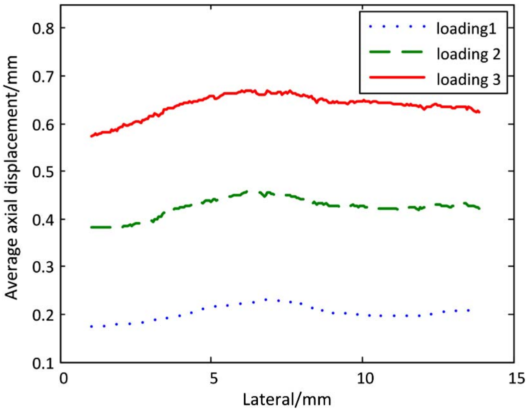

Fig. 8. Average axial displacements along the lateral direction obtained from the three loading conditions with 250 μm incremental axial translation of the actuator.

C. Three Point Bending

The three point bending experiment could be an ideal example to test the axial deformation of structures with OCE. In this study, incremental loadings with 250 μm steps were applied. The cross-sectional images, with 15 mm length symmetrically distributed around the loading point, were acquired for each loading condition. They were processed further to calculate axial displacement maps, as shown in Fig. 7. The white frames indicate the location of the loading post. Figure 8 displays the average axial displacement under each loading condition. It can be seen, from Figs. 7 and 8, that both the local and the integral axial displacement increase around 200–250 μm each time with the incremental loading. The brightest areas in Fig. 7, corresponding to the peak regions in Fig. 8, indicate the locations of the largest displacement. They are in the middle of the imaging area, in a good agreement with the lateral locations of the loading post where the largest displacement theoretically occurs. However, it is worthwhile to note that the distribution of the displacement is not exactly symmetrical. Also in Fig. 7 the maximum axial displacements measured by OCE under the incremental loadings are 238, 476, and 680 μm, respectively, which are slightly less than the physical translations (250, 500, and 750 μm, respectively) of the loading actuator. A most reasonable explanation is due to a small symmetrical error from the setup and the loading. The OCE accuracy and the anisotropic structure of the composite could also contribute to the phenomenon.

4. Discussion

OCE provides information on the internal deformation of materials based on OCT structural images. Therefore the additional elastographic contrast may improve the ability of OCT to characterize the structure of materials. In this study, OCE was applied to glass fiber composite under three different translation or mechanical loadings. From the results shown in Section 3, the first observation is that compared with OCT images, the displacement maps of OCE have better image contrast, which more clearly shows the internal structure of the composite specimen. The OCT images rely on the depth-resolved optical reflectivity from the specimen. Due to the extremely close refractive indices of the glass fiber and the resin (both of which are close to 1.55 [26]), the reflections from inside the glass fiber composite have a low intensity, resulting in an interference signal just above the noise level, as shown in Figs. 3(a) and 3(b), as well as in Fig. 4. In OCE, the speckle pattern, instead of the reflectivity, is tracked to quantify the displacement from the OCT images. Therefore in Figs. 3(c) and 3(d), as well as Fig. 5, the structure of the glass fiber composite is much more clearly shown. So with this enhanced image contrast, OCT-based elastography can be further applied to characterize defects, such as microcracks and delaminations within the glass fiber composite.

However, it has to be pointed out that the OCE spatial resolution is lower than that of OCT due to the use of the processing window, and this resolution decreases with the growing size of the window, as shown in Fig. 5. The larger window sizes tend to average out differences in displacements in a region, resulting in less noisy displacement maps but with reduced spatial resolution. From Figs. 6(b) and 6(c) it can be seen that statistically the measurement accuracy improved dramatically when increasing the window sizes from $20 * 20$ to $40 * 40$. The measured mean displacement improved from 231 to 243 μm, equivalently to a drop in PE from 7.6% to 2.8%. The RMSE decreases from 31 to 20 μm correspondingly. Afterward, there is no significant improvement from further increasing the window size. Finally a size of $50 * 50$ was found to be a good compromise between measurement accuracy and spatial resolution.

Besides the processing window size, the measurement accuracy could also be affected by the OCT image noise, out-of-plane displacement, and speckle decorrelation [27]. For the OCT image noise, a threshold was set to filter out the areas with low signal-to-noise ratio (SNR), which indicate resin-rich areas and areas outside the specimen. These areas in the OCT images are excluded from displacement calculation. The out-of-plane displacement is not studied in this paper. But it is possible to determine using a similar speckle tracking technique or digital volume correlation (DVC) on pairs of volumetric OCT images [28]. The most troublesome factor is speckle decorrelation. The cross-correlation approach of OCE has a limited ability to track the deformations that are either too small or too large. For example, when the speckle motion is only a fraction of a pixel, the cross-correlation approach cannot track the shift robustly even with various smoothing techniques [29]. At the other extreme, the relative positions of the scatterers that form the speckle patterns change gradually when the deformation increases, which results in gradual speckle decorrelation. However, unlike speckles in soft tissues that are easily decorrelated by a small deformation on the order of OCT spatial resolution [30], speckle patterns from composites can endure much larger displacements as presented in this paper. An explanation could be that the areas with fiber reinforcement are stiffer than the polymer matrix areas. So the areas with fiber bundles, where speckles occur, behave more like rigid bodies that translate without deformation. That is why speckles can still be tracked after hundreds of micrometers of displacement. Nevertheless, speckle decorrelation is an inevitable phenomenon during the loading test of a specimen. The improvement on the tracking accuracy and measurement range [31,32] could be a direction for future work.

As the results in Fig. 7 illustrate, a sequence of displacement maps of a glass fiber composite under gradually increasing loading can provide sufficient information to observe the structural variations or even to deduce the regional stiffness by a knowledgeable observer without further processing. However, to estimate a sample's depth-resolved elastic properties quantitatively, local strain needs to be calculated based on the displacement maps. Currently, the method of least squares (LS) has been proved to be a robust approach for the strain estimate in OCE [33]. A set of displacement data in a neighboring region is used to calculate local strain from LS fitting. However, unlike the tissues that can provide consecutive scatterers in a cross-sectional area, optical reflections within glass fiber composite only occur at the fiber–resin interfaces, resulting in discrete speckle patterns separated by the resin-rich areas in OCT images. Consequently, displacement maps, as shown in Section 3, can only display the local results discretely, which makes it difficult to estimate the strain distribution. A possible solution is to mix small inclusions with epoxy to track the displacements from the resin as well. But care must be taken to minimize the influence of the inclusions to the composite elastic properties.

5. Conclusions

This study explored the use of OCE for the deformation measurement of glass fiber composites, for the first time to the best of our knowledge. The developed OCE system can track internal displacements in the range from a few micrometers to hundreds of micrometers. The cross-sectional displacement maps clearly show the structural features and structural variations, which could provide supplementary understanding of the mechanical properties of glass fiber composites.

References

1. R. Rowlands and I. Daniel, "Application of holography to anisotropic composite plates," Exp. Mech. **12**, 75–82 (1972).
2. J. Butters and J. Leendertz, "Speckle pattern and holographic techniques in engineering metrology," Opt. Laser Technol. **3**, 26–30 (1971).
3. D. Post, B. Han, and P. Ifju, "Moiré interferometry," in *High Sensitivity Moiré* (Springer, 1994), pp. 135–226.
4. T. Chu, W. Ranson, and M. Sutton, "Applications of digital-image-correlation techniques to experimental mechanics," Exp. Mech. **25**, 232–244 (1985).
5. Y. Okabe, S. Yashiro, T. Kosaka, and N. Takeda, "Detection of transverse cracks in CFRP composites using embedded fiber Bragg grating sensors," Smart Mater. Struc. **9**, 832–838 (2000).
6. J. Botsis, L. Humbert, F. Colpo, and P. Giaccari, "Embedded fiber Bragg grating sensor for internal strain measurements in polymeric materials," Opt. Lasers Eng. **43**, 491–510 (2005).
7. J. Ophir, I. Cespedes, H. Ponnekanti, Y. Yazdi, and X. Li, "Elastography: a quantitative method for imaging the elasticity of biological tissues," Ultrason. Imag. **13**, 111–134 (1991).
8. C. L. De Korte, G. Pasterkamp, A. F. Van Der Steen, H. A. Woutman, and N. Bom, "Characterization of plaque components with intravascular ultrasound elastography in human femoral and coronary arteries in vitro," Circulation **102**, 617–623 (2000).
9. A. Manduca, T. E. Oliphant, M. Dresner, J. Mahowald, S. Kruse, E. Amromin, J. P. Felmlee, J. F. Greenleaf, and R. L. Ehman, "Magnetic resonance elastography: non-invasive mapping of tissue elasticity," Medical Image Anal. **5**, 237–254 (2001).
10. Q. Zhou, S. Lau, D. Wu, and K. K. Shung, "Piezoelectric films for high frequency ultrasonic transducers in biomedical applications," Prog. Mater. Sci. **56**, 139–174 (2011).
11. L. Massey, M. Miranda, L. Zrinzo, O. Al-Helli, H. Parkes, J. S. Thornton, P.-W. So, M. White, L. Mancini, and C. Strand, "High resolution MR anatomy of the subthalamic nucleus: imaging at 9.4 T with histological validation," Neuroimage **59**, 2035–2044 (2012).
12. D. Huang, E. Swanson, C. Lin, J. Schuman, W. Stinson, W. Chang, M. Hee, T. Flotte, K. Gregory, C. Puliafito, and J. Fujimoto, "Optical coherence tomography," Science **254**, 1178–1181 (1991).
13. B. E. Bouma and G. J. Tearney, *Handbook of Optical Coherence Tomography* (Dekker, 2002).
14. J. M. Schmitt, "OCT elastography: imaging microscopic deformation and strain of tissue," Opt. Express **3**, 199–211 (1998).
15. J. Rogowska, N. Patel, S. Plummer, and M. Brezinski, "Quantitative optical coherence tomographic elastography: method for assessing arterial mechanical properties," Br. J. Radiol. **79**, 707–711 (2006).
16. H.-J. Ko, W. Tan, R. Stack, and S. A. Boppart, "Optical coherence elastography of engineered and developing tissue," Tissue Eng. **12**, 63–73 (2006).
17. B. F. Kennedy, K. M. Kennedy, and D. D. Sampson, "A review of optical coherence elastography: fundamentals, techniques and prospects," IEEE J. Sel. Top. Quantum Electron. **20**, 1–17 (2014).
18. P. Liu, R. M. Groves, and R. Benedictus, "Signal processing in optical coherence tomography for aerospace material characterization," Opt. Eng. **52**, 033201 (2013).
19. D. Stifter, "Beyond biomedicine: a review of alternative applications and developments for optical coherence tomography," Appl. Phys. B **88**, 337–357 (2007).
20. J. M. Schmitt, "Optical coherence tomography (OCT): a review," IEEE J. Sel. Top. Quantum Electron. **5**, 1205–1215 (1999).
21. P. H. Tomlins and R. K. Wang, "Theory, developments and applications of optical coherence tomography," J. Phys. D **38**, 2519–2535 (2005).
22. D. D. Duncan and S. J. Kirkpatrick, "Processing algorithms for tracking speckle shifts in optical elastography of biological tissues," J. Biomed. Opt. **6**, 418–426 (2001).
23. R. K. Wang, S. Kirkpatrick, and M. Hinds, "Phase-sensitive optical coherence elastography for mapping tissue microstrains in real time," Appl. Phys. Lett. **90**, 164105 (2007).
24. P. Liu, R. M. Groves, and R. Benedictus, "Optical coherence tomography for the study of polymer and polymer matrix composites," Strain, doi: 10.1111/str.12095 (to be published).
25. J. Rogowska, N. Patel, J. Fujimoto, and M. Brezinski, "Optical coherence tomographic elastography technique for measuring deformation and strain of atherosclerotic tissues," Heart **90**, 556–562 (2004).
26. G. Elert, "The physics hypertextbook," 2006, http://physics.info/refraction/.
27. C. Sun, B. Standish, B. Vuong, X.-Y. Wen, and V. Yang, "Digital image correlation-based optical coherence elastography," J. Biomed. Opt. **18**, 121515 (2013).

28. J. Fu, M. Haghighi-Abayneh, F. Pierron, and P. Ruiz, "Assessment of corneal deformation using optical coherence tomography and digital volume correlation," in *Mechanics of Biological Systems and Materials*, Vol. **5** (Springer, 2013), pp. 155–160.
29. K. Parker, M. Doyley, and D. Rubens, "Imaging the elastic properties of tissue: the 20 year perspective," Phys. Med. Biol. **56**, R1–R29 (2011).
30. C. Sun, B. Standish, and V. X. Yang, "Optical coherence elastography: current status and future applications," J. Biomed. Opt. **16**, 043001 (2011).
31. S. J. Kirkpatrick, R. K. Wang, and D. D. Duncan, "OCT-based elastography for large and small deformations," Opt. Express **14**, 11585–11597 (2006).
32. V. Y. Zaitsev, L. A. Matveev, G. V. Gelikonov, A. L. Matveyev, and V. M. Gelikonov, "A correlation-stability approach to elasticity mapping in optical coherence tomography," Laser Phys. Lett. **10**, 065601 (2013).
33. B. F. Kennedy, S. H. Koh, R. A. McLaughlin, K. M. Kennedy, P. R. Munro, and D. D. Sampson, "Strain estimation in phase-sensitive optical coherence elastography," Biomed. Opt. Express **3**, 1865–1879 (2012).